Computational Aerodynamic Analysis of Blended Wing Body Aircraft

R.Devaraju[1], R.Naveen kumar[2], J.Naresh[3]

[1] Assistant professor, Aeronautical Engineering, GNITC, Telangana, INDIA
[2] Assistant professor, Aeronautical Engineering, GNITC, Telangana, INDIA
[3] Assistant professor, Aeronautical Engineering, GNITC, Telangana, INDIA

---***---

Abstract: The present research deals with the computational aerodynamic Analysis of BWB at subsonic speeds using Ansys CFD as a simulation tool and ICEM CFD as modeling tool at different angle of attacks and freestream velocities. The study will focus on the aerodynamic characteristics such as mach number and pressure variation over the body, from these results we can find the aerodynamic efficiency(lift force to drag force ratio) so that we can compare the performance characteristics with conventional aircraft.

Key Words: Blended Wing Body (bwb), Hybrid wing, tetra mesh , etc…

1. Introduction

The Blended-Wing-Body (BWB) aircraft are being investigated and researched with the aim to develop more efficient aircraft configurations. The BWB configuration designates an alternative aircraft configuration where the wing and fuselage are integrated which results essentially in a hybrid flying wing shape. BWB is a hybrid of flying-wing aircraft and the conventional Aircraft where the body is designed to have a shape of an airfoil and carefully streamlined with the wing to have a desired plan form.

1.1 Modelling and Meshing in ICEM CFD

Select the front plane (XZ plane) as the reference plane. FILE-IMPORT GEOMETRY-FORMATED POINT DATA
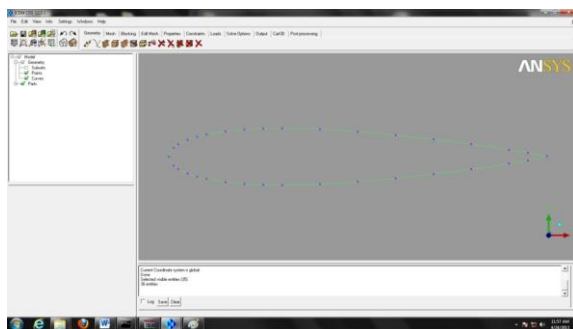

Fig.1.1 Air foils curve import for BWB

1.1.2 Transform Geometry: Tranform geometry using following tools

- Translation

- Rotation
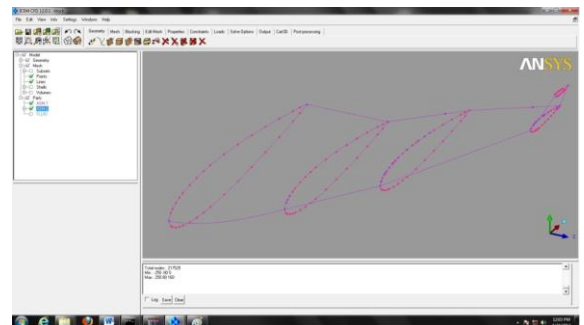
- Mirror Geometry

- Scale Geometry

Fig.1.1 create curves required

1.1.3 Create/Modify Surface Options:

The **From Curves** option allows you to create surfaces from curves. The following options are available for creating surfaces from curves.
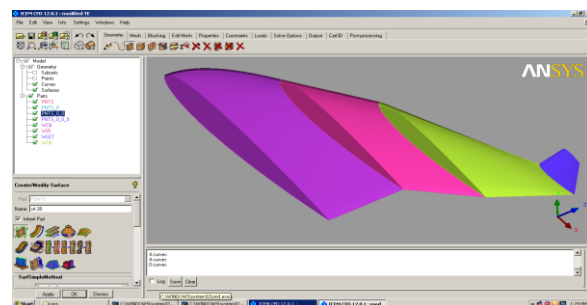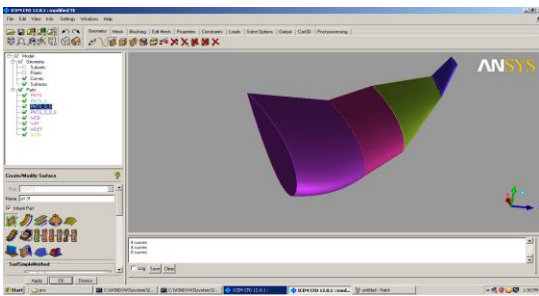

Fig.1.2 Creating airfoil surfaces

Fig.1.3 Half BWB surface

Fig.1.4 3d model with domain

Fig.1.5 Parts of domain: inlet, outlet, symmetry, body

1.2 Mesh:

➢ Global Mesh Setup

➢ Part Mesh Setup(The **Part Mesh Setup** option opens a dialog where we can specify the mesh

  parameters for different parts)

➢ Surface Mesh Setup

➢ Curve Mesh Setup

➢ Create Mesh Density

➢ Define Connectors

➢ Mesh Curve

Compute Mesh(The **Compute Mesh** option allows you to generate the mesh specified by the mesher and various parameters.)

1.2.1 Type of grid :

The Tetra mesher can use different meshing algorithms to fill the volume with tetrahedral elements and to generate a surface mesh on the object surfaces. You can define prescribed curves and points to determine the positions of edges and vertices in the mesh. For improved element quality, the Tetra mesher incorporates a powerful smoothing algorithm, as well as tools for local adaptive mesh refinement and coarsening. The Tetra mesher is suitable for complex geometries, and offers several advantages, including:

➢ Rapid model setup
➢ Mesh independent of underlying surface topology
➢ No surface mesh necessary
➢ Generation of mesh directly from CAD or STL surfaces
➢ Definition of element size on CAD or STL surfaces
➢ Control over element size inside a volume
➢ Nodes and edges of tetrahedra are matched to prescribed points and curves
➢ Curvature/Proximity Based Refinement automatically determines tetrahedra size for individual geometry features
➢ Volume and surface mesh smoothing, merging nodes and swapping edges
➢ Tetrahedral mesh can be merged into another tetra, hexa or hybrid mesh and then can be smoothed
➢ Coarsening of individual material domains
➢ Enforcement of mesh periodicity, both rotational and translational
➢ Surface mesh editing and diagnostic tools
➢ Local adaptive mesh refinement and coarsening
➢ One consistent mesh for multiple materials
➢ Fast algorithm: 1500 elements/second
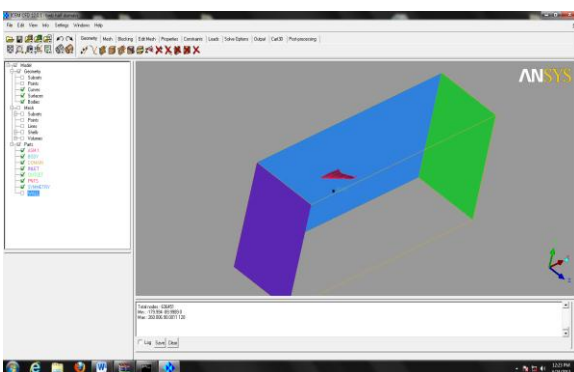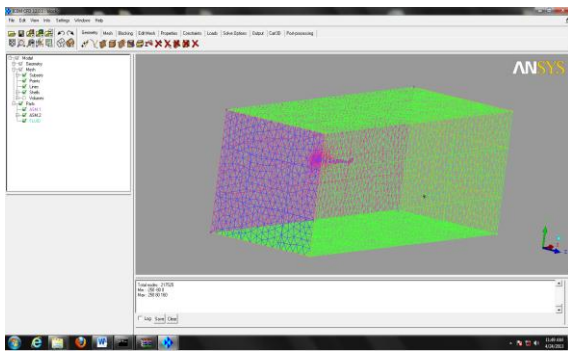➢ Automatic detection of holes and easy way to repair the mesh

Fig.1.6 Meshed Domain
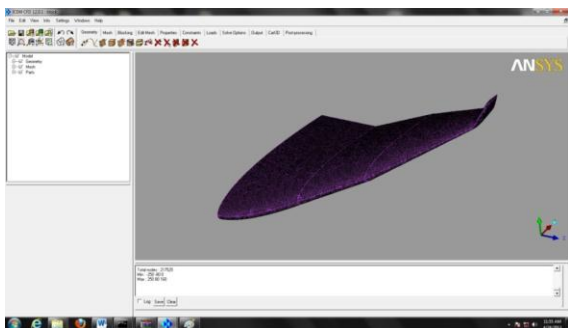

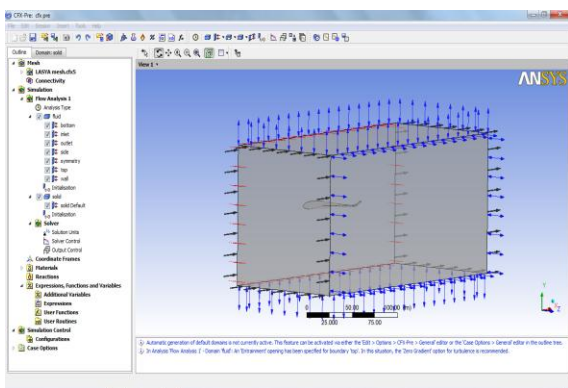**Fig.1.7** 3d BWB control volume with mesh

Fig.1.8 3d cfx-pre setup, initial and boundary conditions.

2. Boundary Conditions

The surface of the projectile is set as an adiabatic wall under no-slip conditions. The inlet and outlet boundary condition are set as free-stream conditions while a symmetry condition is applied at the centerline axis of the projectile. The rest of the control surfaces are set as

opening. The default flow field is set as free-stream conditions.
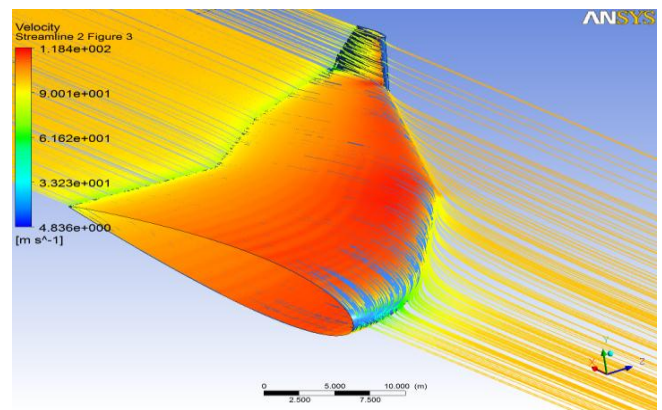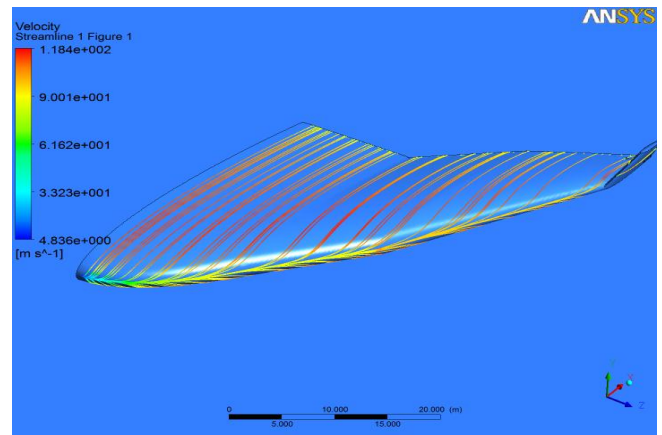
3. Result analysis:
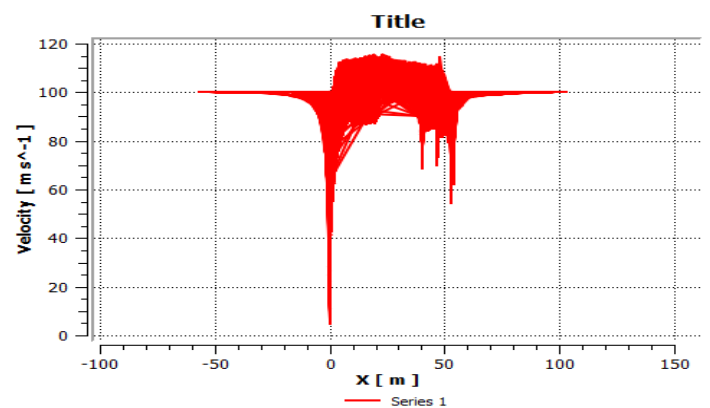

Fig 3.1 streamlines for Mach 0.3, AOA 0^0

Fig 3.1 Velocity variation along body Mach 0.3, AOA 0^0
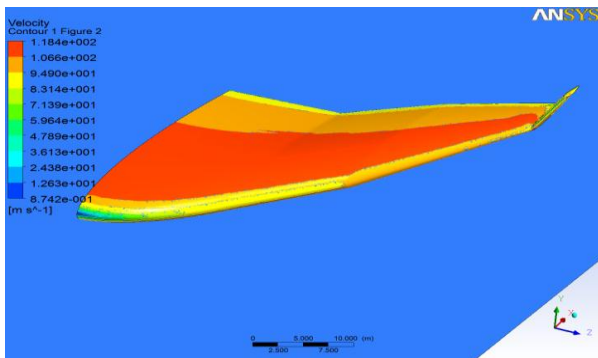
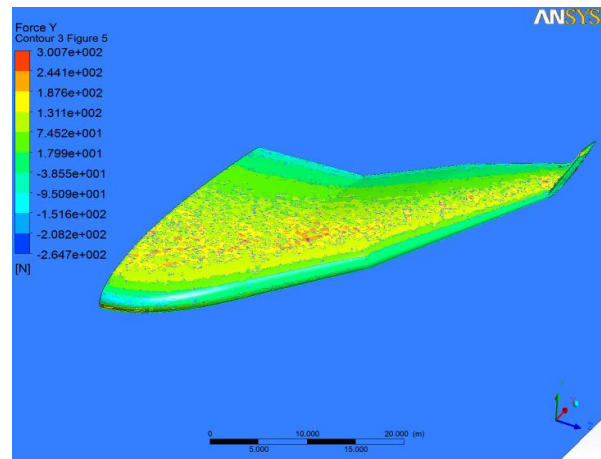**Fig 3.2** Velocity contours Mach 0.3, AOA 0^0

Fig 3.3 Pressure contours for Mach 0.3, AOA 0^0
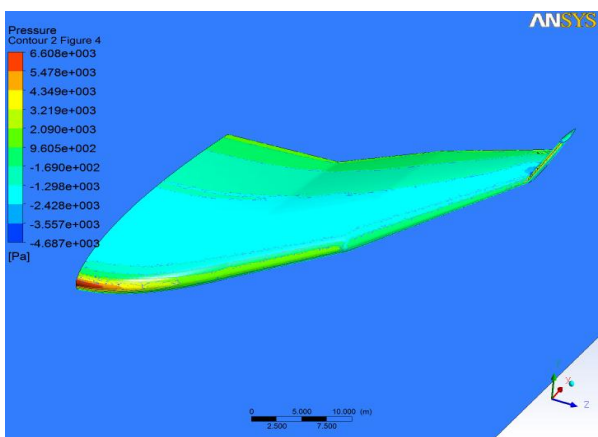

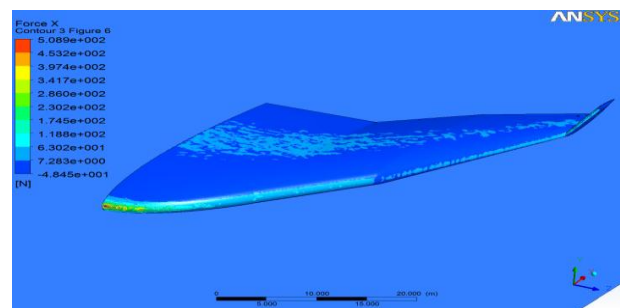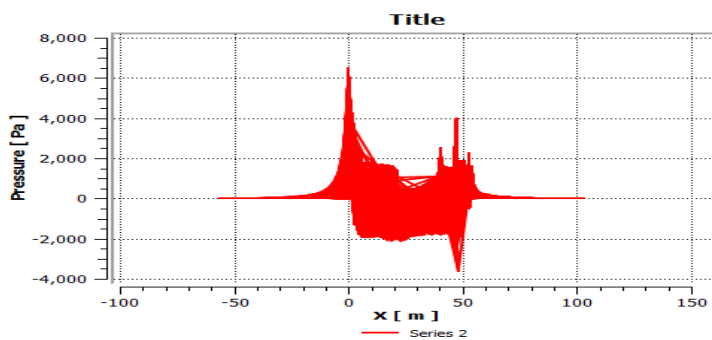**Fig 3.4** Force Y contours for Mach 0.3, AOA 0^0

Fig 3.5 Force contours X for Mach 0.3, AOA 0^0

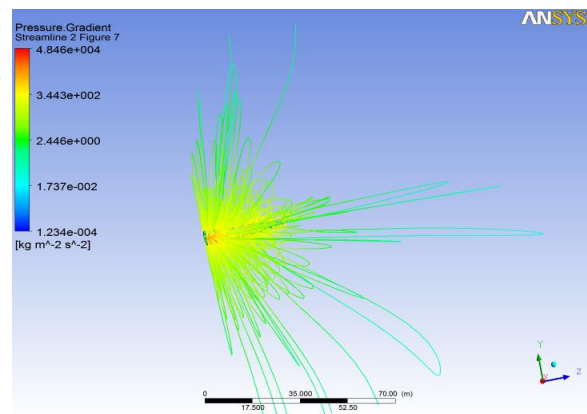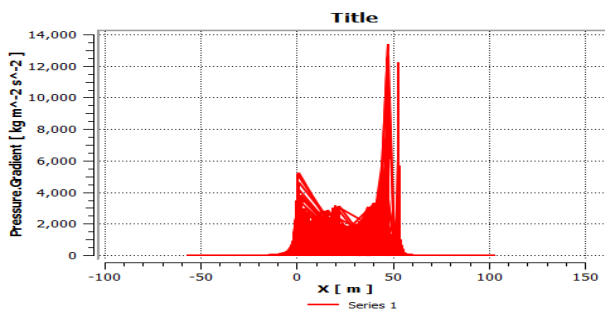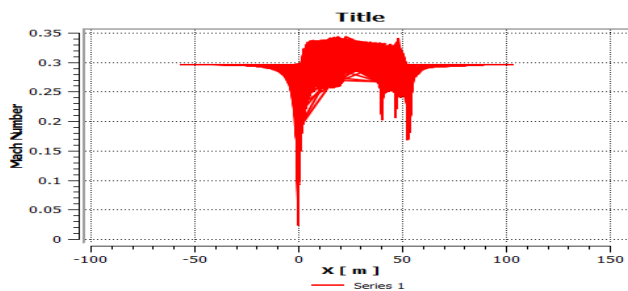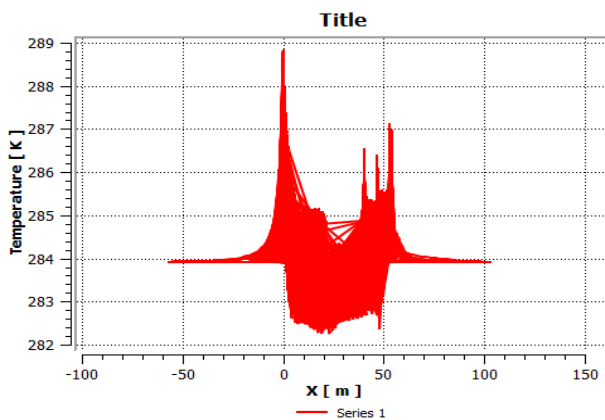**Graph.3.1** Pressure variation along body for Mach 0.3, AOA 0^0

Fig 3.6 Pressure Gradient for Mach 0.3, AOA 0^0

Graph 3.2 Pressure Gradient along body Mach 0.3, AOA 0^0

Graph 3.3 Mach number along body Mach 0.3, AOA 0^0

Graph.3.4 Temperature along body Mach 0.3

Fy and Fx obtained from the CFX simulations represents the axial and normal force respectively. At zero angle of attack, Fy and Fx are equivalent to the lift (FL) and drag force (FD) respectively.

$$F_D = F_x \cos\alpha + F_y \sin\alpha$$

$$F_L = F_y \cos\alpha - F_x \sin\alpha$$

After obtaining Fy, Fx and the torque with respect to z-axis (Tz), the results for CL and CD at various angles of attack were derived using below equations we can find

$$C_L = \frac{2F_L}{\frac{1}{2}\rho V^2 S_{ref}}$$

$$C_D = \frac{2F_D}{\frac{1}{2}\rho V^2 S_{ref}}$$

$$C_M = \frac{2T_z}{\frac{1}{2}\rho V^2 S_{ref}l_{ref}}$$

$$C_{N\alpha} = \frac{C_{N(\alpha_2)} - C_{N(\alpha_1)}}{\alpha_2 - \alpha_1}$$

$$C_{M\alpha} = \frac{C_{M(\alpha_2)} - C_{M(\alpha_1)}}{\alpha_2 - \alpha_1}$$

Graph 3.5 C_L Versus Alpha

Variable	Units	Inlet	Outlet	Symmetry	Body
Velocity	M/s	1.0e+2	1.0e+2	1.010e+2	1.18e+2
Pressure	Pa	0.0e+0	0.0e+0	9.600e+1	2.00e+3
Area	M^2	2.5e+4	2.5e+4	7.984e+4	1.83e+3
Mach no	--	3.0e-1	3.0e-1	3.100e-1	3.50e-1
Force-x	N	-3.1e+8	3.1e+8	4.222e-4	2.44e+4
Force-y	N	9.3e-8	-2.4e+4	3.549e-6	2.56e+4
Mass f	Kg/s	3.1e+6	-3.1e+6	8.119e-6	Na
Temp	K	2.8e+2	2.8e+02	2.880e+2	2.82e+2

Table 3.1 Analysis report Mach 0.3, AOA 0^0
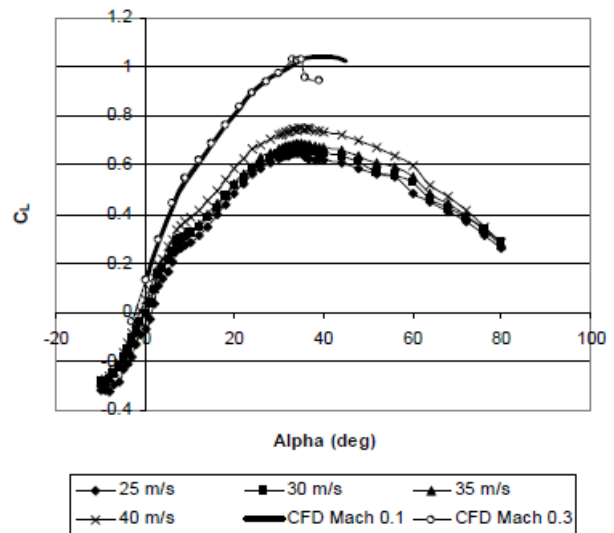
AIRFOIL	Drag Coefficient C_D	Lift Coefficient C_L	L/D
NACA0015	0.00736	0.15770	21.43
NACA64-206	0.00693	0.15096	21.80

Table 3.2 Comparison between the NACA0015 and the NACA64-206 Models of CFD Results
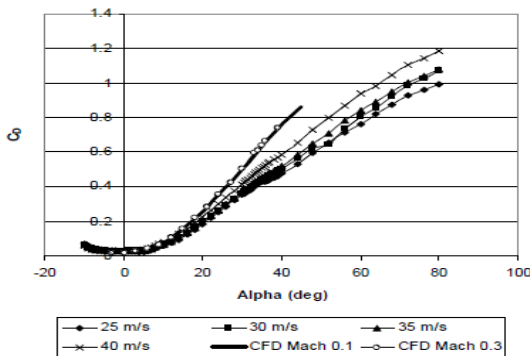
Graph 3.6 C_D Versus Alpha

3.1 Lift Coefficient Analysis:

Graph 3.5 shows variation of lift coefficient (C_L) for different values of angle of attack (α). For given free stream speed, the value of C_L increases as the angle of attack is increased until its maximum value at around α = 3° and decreases afterwards with lower slope. The present Computational Fluid Dynamics (CFD) results at Mach 0.1 and 0.3 also give the similar trend with maximum C_L located at α = 1° and α = 3° respectively.

It is observed that the value of $C_L max$ increases as the Mach number is increased. the $C_L max$ increases with the increase of Reynolds number.

3.2 Drag Coefficient Analysis

Graph 3.6 shows variation of drag coefficient (C_D) versus angle of attack (α) taken at different Mach numbers. It is observed that the variation of drag coefficient is very slow and almost constant at low angles of attack. In that range of α, C_D is small, below 0.03. As explained in the previous section, at low angle of attack, the air flow is still attached to the wing. Above Angle of attack of 8°, C_D grows at higher rate as α is increased.

Within this range, the wing is already in stall condition. Around 8^0, a slight deflection occurs on wind tunnel experiment curves.. Beyond this angle of attack, the drag coefficient continues to increase with almost the same slope as between 8° and 10°, and it is getting slower when α approaches 10°. From the overall curves, it is observed that higher airspeeds (or higher Reynolds number)produce higher drag coefficients
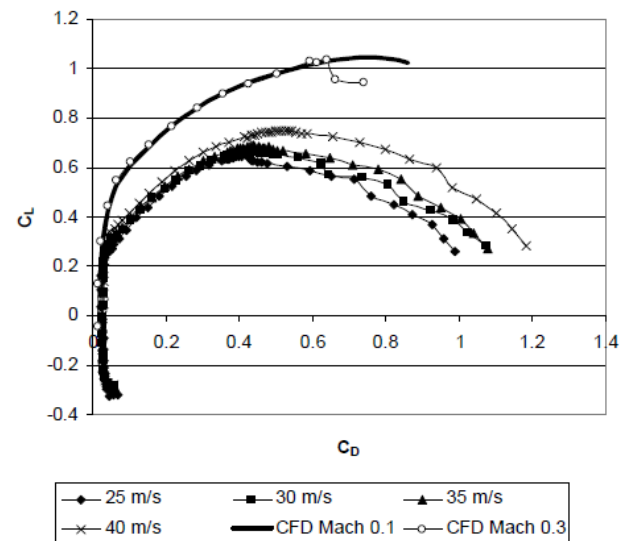
Graph.3.7 C_L versus C_D

3.3 Lift Coefficient versus Drag Coefficient(Drag polar) Analysis

The drag polar (C_L versus C_D) curve can be seen in Graph.3.7. From experimental curves, the value of drag coefficients at zero lift (C_{Do}) is around 0.03. The CFD results give C_{Do} lower than 0.02. This is the minimum drag coefficient that the BWB has without producing any lift. From the curves, it can be seen that when the drag coefficient increases, the lift coefficient increases until its maximum value $C_L max$ and then decreases.
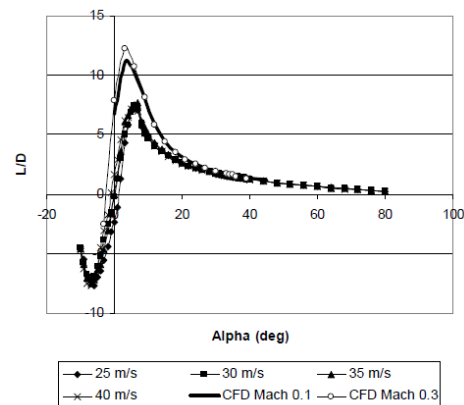
Graph 3.8 L/D ratio versus Angle of attack

3.4 Lift-to-Drag Ratio Analysis

Graph 3.8 shows the curves of lift-to-drag ratio (L/D) as a function of angle of attack (α). It is noticed that, for experimental curves, the lift-to-drag ratio increase from a minimum value of –7.65 at α = –7º to its maximum value of 7.27 at α = 6º. The CFD gives the maximum value of L/D = 11.07 (for Mach 0.1) and L/D = 12.24 (for Mach 0.3) both at α = 3º. These angles of attack (α = 6º from experiments and α = 3º from CFD analysis) indicate the optimum flight configuration of the BWB. These lift-to drag ratios are considered low. Cranfield University with its BWB design manages to have maximum lift-to-drag ratio of 14
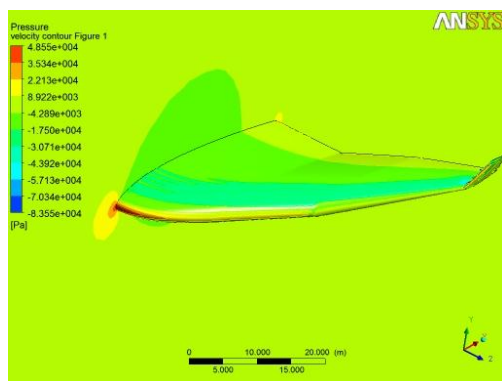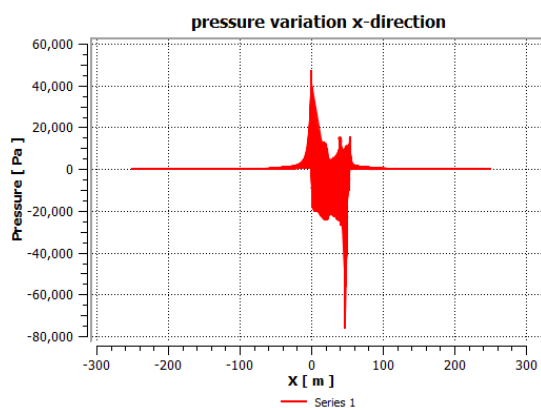
3.4 Analysis-2 for Mach 0.85 and AOA 3⁰:-

Fig.9.10 Pressure contour for Mach 0.85 and AOA 3⁰

Graph 3.9 Pressure variation along x-direction for
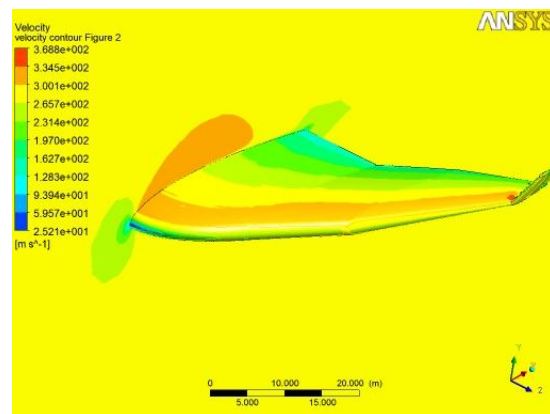
Mach 0.85 and AOA 3⁰

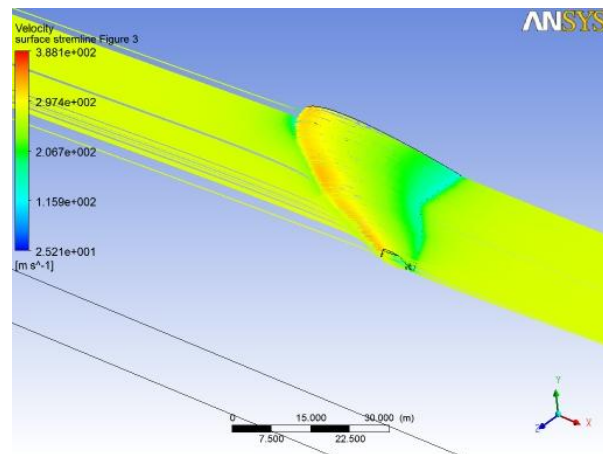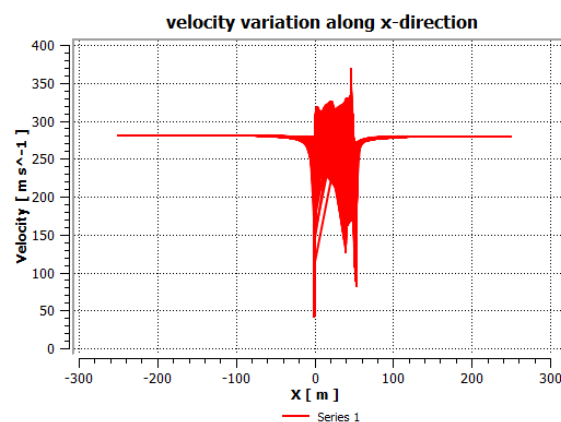## 3.4.1 Pressure Coefficient Contours

Fig3.8 Velocity contours

Fig 3.9 streamline pattern

Graph.3.10 Velocity variation along x-direction
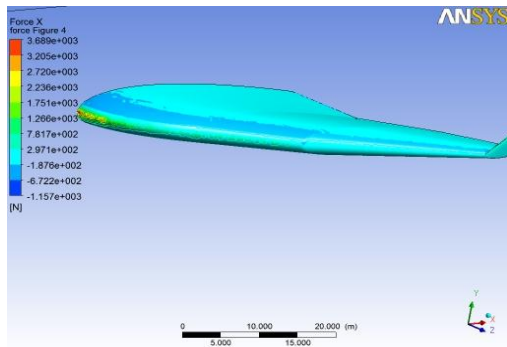
Fig.3.10 Force-x contours

Airfoil	Force-x (N)	Force-y (N)	Lift Coefficient C_L	Drag Coefficient C_D	L/D
NACA 64-206	3.689 e+003	3.580 e+003	0.15296	0.00 695	22.8 0

Table 3.3 Calculation of L/D ratio for
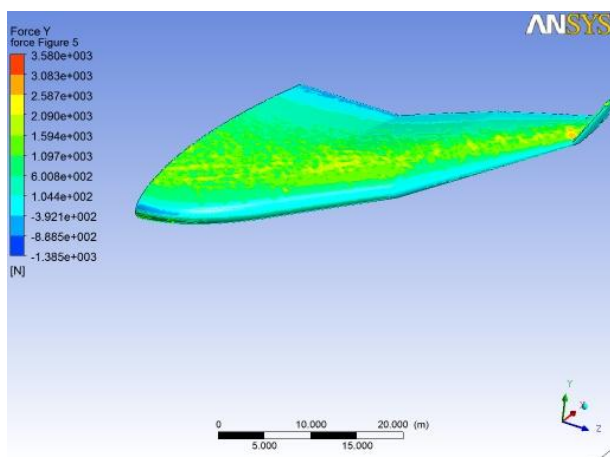
Mach number0.85, AOA3[0]

Fig 3.11 Contours of Force Y

3.5 Velocity Contours and Streamlines

The velocity contours of BWB at 0.3, 0.85 Mach numbers are shown in Fig. 9.2 and Fig.9.11 respectively. Increasing angles of attack will cause the Mach number on upper surface to increase while simultaneously decreasing on the lower surface. This results in the lift coefficient increasing when angle of attack increases. As angle of attack increases beyond $C_L max$, the flow will eventually separate from the surface. Separation starts from the wing leading edge and spreads towards the trailing edge of the wing. Although the wing does not provide lift at this (α=0), effective flow occurs on the center body resulting in some lift being generated by the high swept leading edge vortex on the body (similar to delta wing).

4. CONCLUSIONS AND FUTURE WORK

In the present study the flow simulation has been carried out for BWB configuration at Mach numbers of 0.1, 0.3 and 0.85 using CFD commercial software ANSYS CFX at different angles of attack. The flow characteristics in terms of velocity contours, pressure contours and streamline pattern are obtained for the BWB At Mach number 0.3 the L/D ratio obtained is 21.43.This is closer to that of Airbus A380. As the angle of attack increases the lift coefficient is found to increases. The streamline patterns obtained show the behavior of the flow over the body. The maximum velocities are found to occur at around quarter chord of the body. From the pressure contours obtained it can be seen that maximum pressure occurs in the nose region. The results obtained are useful for both UAV and commercial BWB flight configurations. The BWB configuration is an alternative aircraft configuration where the wing and fuselage are integrated which results essentially in a hybrid flying wing shape. The BWB design seems to show greater potential for very large passenger transport aircraft.

The present study can be extended to CFD based design optimization of BWB configuration.

REFERENCES
[1] Liebeck, R. H., "Design of the Blended-Wing-Body Subsonic Transport," 2002 Wright Brothers Lecture, AIAA Paper 2002-0002, Jan. 2002.
[2] Liebeck, R. H., Page, M. A., Rawdon, B. K., "Blended-Wing-Body Subsonic Commercial Transport," AIAA Paper 98-0438, Jan. 1998.
[3] "Blended-Wing-Body Technology Study," Final Report, NASA Contract NAS1-20275, Boeing Report CRAD-9405-TR-3780, Oct. 1997.
[4] http://cfl3d.larc.nasa.gov/Cfl3dv6/cfl3dv6.html